High-frequency forcing to mitigate unsteady separation from a bursting separation bubble

Stuart I. Benton and Miguel R. Visbal

Phys. Rev. Fluids **3**, 013907 — Published 29 January 2018

DOI: 10.1103/PhysRevFluids.3.013907

High-frequency forcing to mitigate unsteady separation from a bursting separation bubble

Stuart I. Benton* and Miguel R. Visbal
Air Force Research Laboratory, Wright-Patterson AFB, OH 45433
(Dated: January 17, 2018)

The ability for high-frequency, low-amplitude forcing to delay the onset of unsteady separation due to bursting of a small laminar separation bubble is considered through the use of large eddy simulation. The study begins with the static flow over a NACA 0012 airfoil at $\alpha = 8^\circ$ and $Re_c = 2\times10^5$. The ability for the laminar separation bubble to act as a spatial amplifier of select frequencies is documented. Sinusoidal or pulsed forcing within this frequency range is shown to reduce the length of the separated region. Boundary layer transition is shown to occur due to a short-wavelength secondary instability, the behavior of which is sensitive to the properties of the shed vortex structures. Control is then applied to the case of a constant-rate pitch-up motion to evaluate the potential for delay of dynamic stall onset. During the pitch up motion the most amplified shear layer frequency increases due to flow acceleration and reduced separation length scale. The most effective control scenarios using sinusoidal, pulsed, or variable frequency approaches are shown to continually energize the laminar separation bubble throughout the pitching motion until turbulent separation propagates to the leading edge.

* stuart.benton.ctr@uf.af.mil

I. INTRODUCTION

The complexity of the fluid mechanisms associated with unsteady separation on a moving airfoil have been the subject of considerable research over the past half-century[1–3]. Large force and moment oscillations associated with these events can be detrimental to aircraft stability. Negative pitch-damping can result in un-damped oscillations that risk structural damage. The sensitivity of the process to motion parameters, flow parameters, and the state of the airfoil boundary layer makes successful prediction difficult.

Within a wide range of Reynolds number the airfoil boundary layer may exhibit a small laminar separation bubble (LSB) induced by a strong adverse pressure gradient. The role of this feature in the dynamic stall process was first noted by Ham[4] on the NACA 0012 airfoil. The bubble was shown to contract with increasing incidence until it suddenly burst resulting in the shedding of a large dynamic stall vortex from the airfoil leading edge. The advection of this vortex structure over the surface of the airfoil causes a strong increase in the lift coefficient along with a large transient nose-down moment[5, 6]. This process appears to be particularly severe on the NACA 0012 airfoil[7, 8], however symmetric airfoils of similar thickness are still of interest for practical use due to very little movement in the center of pressure during changes in angle of attack[9].

Active control of dynamic stall has been approached through a variety of methods[10–12]. Using periodic excitation, these approaches typically rely on momentum injection at reduced frequencies of $O(1)$ and momentum coefficients at $O(1\%)$ to directly mitigate separation development throughout the unsteady maneuver. Control that specifically targets shear layer instabilities to reduce the size of the LSB has only been studied in static flow situations[13–17]. The targeting of convective instability mechanisms to change the boundary layer state is particularly attractive due to the natural amplification of input energy[18].

The use of high-fidelity simulations such as large eddy simulation to model the dynamic stall process has recently been introduced by Visbal[19] for Reynolds numbers of $2 \times 10^5 - 5 \times 10^5$. The sensitivity of the dynamic stall process to the state of the boundary layer prior to stall requires modeling techniques that capture the laminar, turbulent, and transitional features of the boundary layer. With a focus on mitigating bubble bursting, Visbal[20] applied high frequency forcing from a leading edge strip. Control was introduced with a pulsed waveform at a non-dimensional frequency of $St = 50$ and was shown to be highly effective for the case of a constant-rate pitch-up motion. This approach was extended to the case of sinusoidal pitching and was shown to completely eliminate leading edge separation for both light and deep dynamic stall cases[21]. This resulted in significant improvements in cycle-averaged drag and eliminated negative net-cycle pitch damping as compared to the uncontrolled case. An extension to a finite-aspect ratio wing[22, 23] has also been presented, further confirming the applicability of this approach.

The use of a limited spanwise domain to minimize grid requirements is a common practice in large eddy simulation. Visbal and Garmann[24] compared this flow configuration with common wind-tunnel configurations including a fixed endwall and various end gap arrangements. It was shown that the spanwise-periodic simulation was able to accurately predict the *onset* of dynamic stall (i.e. leading edge bubble bursting). The downstream development of the dynamic stall vortex and the reattachment process were highly dependent on spanwise end effects and long-wavelength behaviors not captured in the truncated domain.

The current investigation is a considerable extension of the work presented in Benton and Visbal[25] and seeks to isolate the mechanisms responsible for the effectiveness of high-frequency forcing at delaying the onset of dynamic stall. Using large eddy simulations of the flow over a NACA 0012 airfoil the effect of forcing frequency and waveform is investigated beginning with the static case at $\alpha = 8°$. With this improved understanding, a study of dynamic stall during a constant-rate pitch-up motion is evaluated. The effectiveness of each of the proposed frequency and waveform computations are considered. Finally, a variable frequency control approach is introduced which tracks the most amplified shear layer frequency throughout the pitching motion.

II. NUMERICAL APPROACH

A. Implicit Large Eddy Simulation

All simulations are performed with the extensively validated high-order Navier-Stokes solver *FDL3DI*[26, 27]. In this code, a finite-difference approach is employed to discretize the governing equations, and all spatial derivatives are obtained with sixth-order compact-differencing schemes[28]. At boundary points, high-order one-sided formulas are utilized which retain the tri-diagonal form of the scheme. Neumann boundary conditions are implemented with third-order one-sided expressions. Time-marching is accomplished through the second-order, iterative, implicit, approximately-factored Beam and Warming method[29].

The governing equations are the fully three-dimensional, compressible, unfiltered, Navier-Stokes equations. The equations are cast in the strong conservative form utilizing a general time-dependent curvilinear coordinate transfor-

mation from physical to computational space, $(x, y, z, t) \rightarrow (\xi, \eta, \zeta, \tau)$[30, 31]. Pressure, density, and temperature are related through the ideal gas law. The equations are non-dimensionalized by the free stream velocity (U_∞) and the airfoil chord (c), with the exception of static pressure which is non-dimensionalized by twice the free-stream dynamic pressure $\rho_\infty U_\infty^2$. All results follow this same non-dimensionalization unless otherwise specified.

For the case of a pitching airfoil, the grid is moved in a rigid fashion using the prescribed airfoil motion. To ensure that the Geometric Conservation Law is satisfied, the time metric terms are evaluated employing the procedures described in Visbal and Gaitonde[32].

In order to eliminate spurious components, a high-order lowpass spatial filtering technique[26, 33] is introduced. A compact formulation based on templates proposed by Lele[28] and by Alpert[34] and with proper choice of coefficients, provides a $2N$th-order formula on a $2N+1$ point stencil. The $N+1$ coefficients are derived using Taylor- and Fourier-series analysis. Theses coefficients, along with representative filter transfer functions, can be found in Gaitonde and Visbal[27, 35]. The filter is applied to the conserved variables along each transformed coordinate direction once after each time step or sub-iteration. For the near-boundary points, the filtering strategies described in Visbal and Gaitonde[26] are used.

The above numerical methods are applied to the original *unfiltered* Navier-Stokes equations, and are used without change in laminar, transitional or fully turbulent regions of the flow. For transitional and turbulent regions, these high-fidelity spatial algorithmic components provide an effective implicit large-eddy simulation (LES) approach in lieu of traditional sub-grid stress models, as demonstrated in Visbal and Rizzetta[36], Rizzetta *et al.*[37], and Garmann *et al.*[38].

B. Linear Stability Analysis

A stability analysis of the boundary layer profiles in the upstream portion of the LSB is performed using the Langley Stability and Transition Analysis Code (LASTRAC)[39]. LASTRAC solves the eigenvalue problem associated with the fully compressible linearized Navier-Stokes equations using a quasi-parallel assumption for the boundary layer region.

For the uncontrolled static flow condition, the linear stability analysis is applied to the wall-normal boundary layer profiles beginning just upstream of the separation point and integrating downstream to the maximum height of the bubble. LASTRAC solves the eigenvalue problem associated with the so called "spatial" problem which assumes a real frequency ($St = fc/U_\infty$) input and a complex eigenvalue which is composed of the streamwise wavenumber and growth rate ($k - i\sigma$). For each streamwise station and each frequency, the most unstable eigenvalue is extracted and saved. For each frequency the amplification rate is integrated using eq. 1 to compute the amplitude growth of an incoming disturbance.

$$A\left(s_h\right) = A_0 exp\left\{\int_{s_0}^{s_h} \sigma\left(s\right) ds\right\} \tag{1}$$

Where s_0 is the initial point of integration (the first station to return an unstable eigenvalue) and s_h is the streamwise station corresponding to the maximum height of the bubble. Data in this context is plotted as $A\left(s_h\right)/A_0$ vs. St in order to approximate the results of a fully global optimal growth analysis such as that performed in Alizard *et al.*[40].

III. PROBLEM SPECIFICATION

A. Preliminary Considerations

Computations are performed for the NACA 0012 wing section. This symmetric section with 12% maximum thickness and leading-edge radius $r_o/c = 0.0158$ has been used in numerous experimental and computational dynamic stall investigations. In order to avoid compressibility effects, a low freestream Mach number $M_\infty = 0.1$ is specified.

The grid is shown in Fig. 1. The original sharp trailing edge was rounded with a very small circular arc in order to facilitate the use of an O-mesh topology. A large O-grid is divided into a system of four nested O-grid blocks. The Chimera overset technique with high-order interpolation[41] is applied to transfer information between grids. This allows for successive coarsening in the azimuthal and spanwise directions in regions far from the airfoil, that would otherwise be restricted to resolution requirements dictated by the turbulent boundary layer. The grid used in this study is a nested version of the single block O-grid presented in Visbal[19] and used in subsequent works[20, 21, 25]. Details concerning grid resolution and validation are included in an appendix provided in the

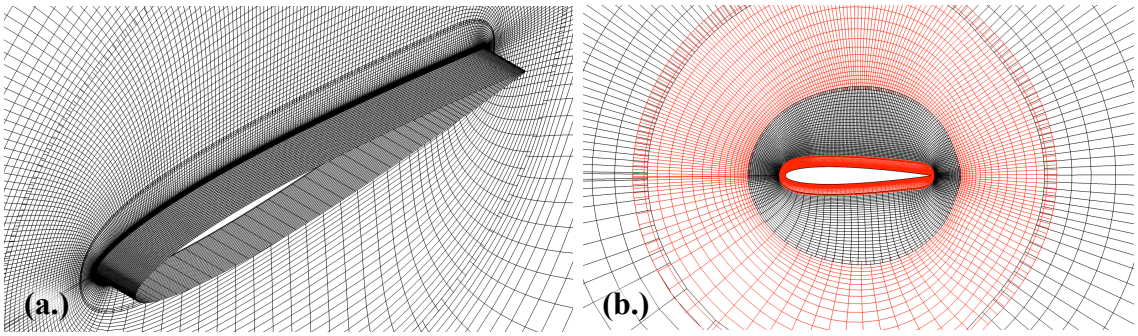

FIG. 1. Isometric (a.) and side (b.) views of the nested O-grid used in the current study. Every fourth grid point is shown.

supplementary material[42]. Where it is shown that the grid resolution conforms to LES resolution requirements put forward in the literature[43, 44]. Sectional 2-D grids were used to construct the three-dimensional mesh which extended a distance $S/c = 0.1$ in the spanwise direction with a uniform Δz spacing. The effects of spanwise extent for this same pitching motion and Reynolds number have been evaluated in Visbal and Garmann[45] where it was shown that $S/c = 0.1$ is sufficient for resolving the flow features relevant to the onset of dynamic stall. An extended discussion on the use of a limited domain is also included in the supplementary material[42].

Boundary conditions are prescribed as follows. Along the airfoil surface, a no-slip adiabatic condition is employed in conjunction with a zero normal pressure gradient. The surface velocity components (u_s, v_s, w_s) are determined from the imposed pitching motion, and are otherwise set to zero for static cases. Along the far field boundary, located 100 chords away from the airfoil, freestream conditions are specified. In the far-field an absorbing sponge zone, as described by Zhou and Wang[46], is introduced. This region is slowly implemented between $50c$ and $70c$ away from the airfoil where it is fully applied to the end of the domain. Spatially-periodic conditions were enforced in both the azimuthal and spanwise (homogeneous) directions using five-plane overlaps.

All computations are performed with a non-dimensional time step of $\Delta t U_\infty/c = 0.00002$ in order to sufficiently resolve small scale turbulent features as well as the input waveforms used for flow control. For pitching simulations the entire flow solution is output every 1000 iterations corresponding to a non-dimensional time of 0.02. Additionally, flow properties on the airfoil suction surface and the three nearest grid planes (in order to compute wall velocity gradients) are saved every 50 iterations corresponding to a non-dimensional time of 0.001.

B. Flow Control

Flow control is implemented using a suction/blowing strip placed on the airfoil pressure surface just below the leading edge. This strip spans from $x/c = 0.0$ to $x/c = 0.002$ and has a length $(s_2 - s_1)/c \approx 0.008$ along the airfoil surface. This location is chosen such that the actuator is upstream of the separation point throughout the entire pitching motion. The wall-normal velocity is prescribed as:

$$v_n/U_\infty = V_{max} \cdot F(t) \cdot G(s) \tag{2}$$

$$G(s) = sin\left[2\pi\left(\frac{s - s_1}{s_2 - s_1}\right)\right] \tag{3}$$

The temporal function, $F(t)$, is prescribed as either a sine wave or in a pulsed form as a square wave with a duty cycle of 50% (see Fig. 2a). For the pulsed waveform, the transitions from on to off are smoothed with a cubic polynomial. These transitions are limited to $1/20^{th}$ of the pulsing cycle. Figure 2b shows the associated Fourier spectrum of each of these waveforms. This highlights the presence of higher harmonics introduced by the pulsing mechanism. Because the duty cycle is fixed at 50%, these harmonics are the odd super-harmonics ($n = 3, 5, 7, ...$) of the fundamental frequency ($n = 1$) and their amplitude decreases proportional to n^{-1}. The effect of the smoothing between transitions acts to damp the higher harmonics, but has no discernible effects on the first two harmonics ($n = 3$ & 5).

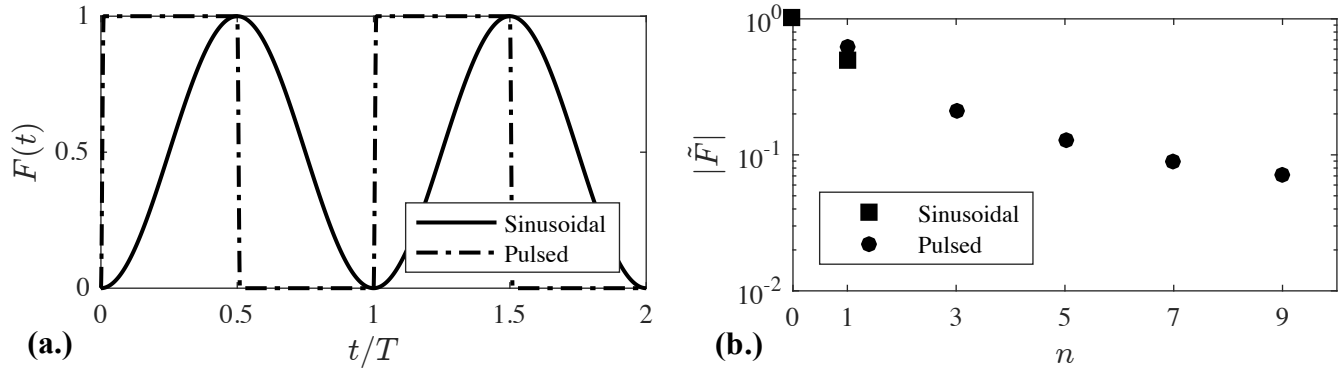

FIG. 2. Waveform comparison (a.) and associated Fourier spectrum (b.) for pulsed and sinusoidal versions of the function $F(t)$.

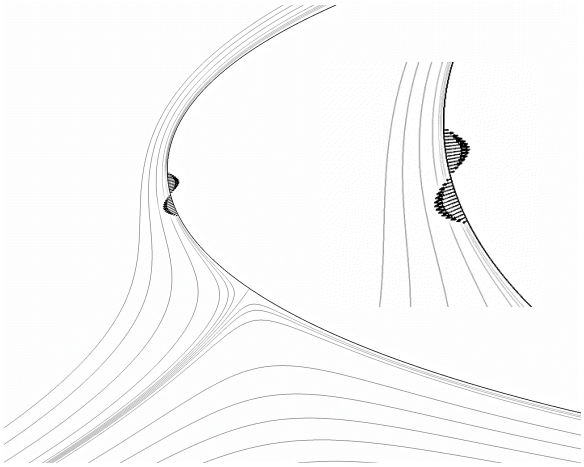

FIG. 3. Velocity profile of the forcing slot as described by the function $G(s)$. Streamlines show the position of the stagnation point relative to the control slot for $\alpha = 8°$.

The forcing strip and its associated velocity profile are shown in Fig. 3 in relation to the instantaneous flow streamlines (light gray) at $\alpha = 8°$. Although the forcing strip is placed on the pressure surface, it is still downstream of the stagnation point within the upper surface boundary layer.

To better compared to the separation control literature, a momentum coefficient can be defined as shown in eq. 4. This results in the relations $C_\mu = 3.8 \times 10^{-3} V_{max}^2$ and $C_\mu = 2.9 \times 10^{-3} V_{max}^2$ corresponding to pulsed and sinusoidal time-functions, respectively. Throughout this study V_{max} has been fixed at the relatively small value of 0.1, which gives momentum coefficients of $C_\mu = 3.8 \times 10^{-5}$ (pulsed) and $C_\mu = 2.9 \times 10^{-5}$ (sinusoidal).

$$C_\mu = 2 \cdot V_{max}^2 \cdot \frac{1}{T} \int_0^T F^2(t)dt \cdot \int_{s_1}^{s_2} G^2(s)ds \tag{4}$$

These values of C_μ ($0.003 - 0.004\%$ in percentage terms) are at least an order of magnitude lower than those surveyed for separation control by Greenblatt and Wygnanski[13]. As will be described in this paper, by properly understanding and accounting for the strong frequency sensitivity of the flow field, it is possible to offer a significant energy cost savings over more classical approaches. By examining the perturbation levels in the boundary layer immediately downstream of the actuator it is observed that the control disturbance only moderately increases the amount of average unsteadiness within the boundary layer. The magnitude of this unsteadiness is shown to *decay* within the region between the actuator and the separation point and falls to the same level as the natural unsteadiness. Therefore, the role of the actuator is primarily a re-ordering of the incoming perturbation profile into narrow bands of frequency.

C. Pitching Motion

This study examines dynamic stall on an airfoil pitching at a constant rate. All solutions are initiated with a statistically stationary solution at $\alpha = 8°$. To avoid infinite acceleration at the initiation of the motion, the angular acceleration is specified to decay exponentially from the finite value of $\Omega_0 4.6/t_0$ to zero (eq. 5). Where Ω_0 is the eventual constant pitch rate and the acceleration decays within the initial time window specified by t_0.

$$\ddot{\alpha}(t) = \Omega_0 4.6/t_0 e^{-4.6t/t_0} \tag{5}$$

Eq. 5 can be integrated once to give the pitch rate (eq. 6) and twice to give the change in angle of attack (eq. 7).

$$\dot{\alpha}(t) = \Omega_0 \left(1 - e^{-4.6t/t_0}\right) \tag{6}$$

$$\alpha(t) = \Omega_0 \left[t + t_0/4.6 \left(e^{-4.6t/t_0} - 1\right)\right] + \alpha_0 \tag{7}$$

Throughout this study the constant pitch-rate is set at $\Omega_0 = 0.05$ and the acceleration decays within the first $t_0 = 0.5$. All pitching motions begin at the initial angle of attack of $\alpha_0 = 8°$. Lorber and Carta[47] showed that for a constant pitch-rate, dynamic stall is independent of the starting α given that it is sufficiently below the static stall angle. Furthermore, the computations of Visbal[19] began at $\alpha_0 = 4°$ and are in excellent agreement with the current study.

IV. RESULTS

A. Uncontrolled Performance

At $\alpha = 8°$ and $Re_c = 2 \times 10^5$ the airfoil boundary layer is characterized by a small LSB ($L/c = 0.1$) near the leading edge which initiates transition to a fully turbulent boundary layer that covers the remainder of the suction surface. The boundary layer on the pressure surface is laminar. This boundary layer topology is unchanged for angles greater than $\alpha = 8°$ up to the point of stall (expected within $12° \leq \alpha \leq 15°$[9, 25]), with the primary difference being a shortening of the LSB length. At this Re_c, the NACA 0012 stall process is characterized as *leading-edge stall*[48], in which the small LSB located near the leading edge of the airfoil abruptly bursts resulting in full boundary layer separation at the leading edge.

Figure 4a shows contours of time-mean vorticity outlining the leading-edge LSB. Transition develops primarily due to a convective Kelvin-Helmholtz instability in the upstream portion of the LSB. Turbulence develops through a combination of non-linear energy transfer to super-harmonics as well as the development of secondary three-dimensional modes which manifest on the large scale structures as well as in the braid region in between[49]. The energy spectrum of velocity fluctuations (Fig. 4b) extracted from points within the shear layer illustrates this process. At the most upstream location ($x/c = 0.06$) high-frequency unsteadiness appears within a small range $40 \leq St \leq 80$. Just downstream, this unsteadiness amplifies and at $x/c = 0.08$ discrete peaks in the $n = 2$ and $n = 3$ super-harmonics of this range also develop. This results in rapid transition to turbulence which takes place in the range $0.09 \leq x/c \leq 0.12$. The energy spectra at the final probe location ($x/c = 0.11$) shows broadband unsteadiness with clear evidence of an inertial range indicated by the $-5/3$ power-law of energy decay.

In corroboration with this analysis of the transition process a linear stability analysis is performed in the upstream portion of the LSB. As described previously, eigenvalue computations are performed at multiple streamwise location starting just upstream of separation ($x/c = 0.018$) and continuing to the point of maximum bubble height ($x/c = 0.085$). The amplification rate is integrated in accordance with eq. 1 to compute amplitude growth through convective instability. The results of this analysis are shown in Fig. 5 as a range of amplified frequency spanning $0 \leq St \leq 90$, with a peak in the vicinity of $St = 50$. This is in close agreement with the frequency spectra (Fig. 4a) results suggesting that convective instability is a key mechanism in the transition process.

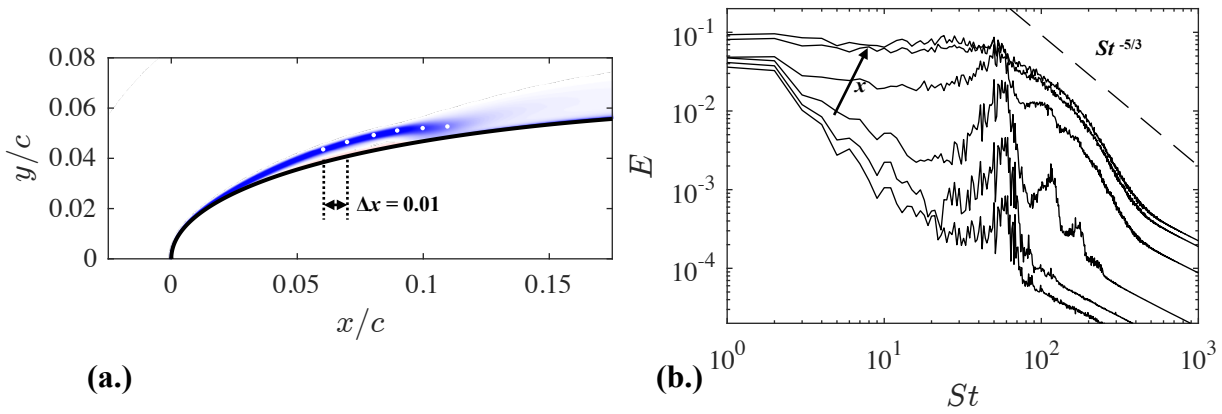

FIG. 4. Contour of time-mean vorticity (a.) of leading edge LSB at $\alpha = 8°$. Turbulent energy spectra (b.) acquired in the shear layer marked by white dots in (a.).

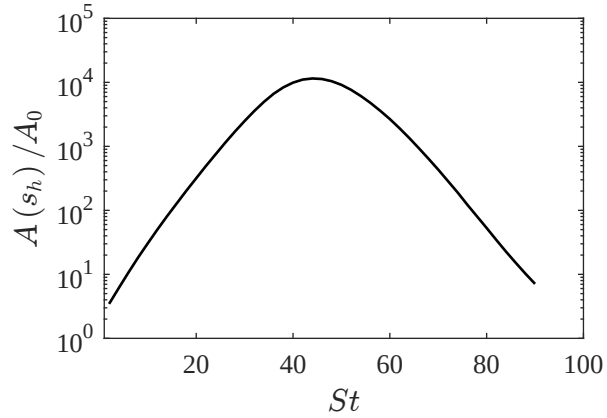

FIG. 5. Amplitude gain as a function of St computed using quasi-parallel linear stability theory.

B. Forcing Effectiveness

1. *Effect of St*

The effect of forcing frequency is evaluated in detail for the static case at $\alpha = 8°$. The response of the boundary layer to forcing is first investigated by looking at instantaneous snapshots of the q-criterion vortex identification function. Figure 6 shows a top-down view of the airfoil leading edge. Iso-surfaces of q-criterion colored by velocity magnitude are used to highlight the response of the LSB to sinusoidal forcing and illustrate the transition to three-dimensional turbulence. Forcing is applied at five frequencies centered about the range of the most amplified frequency (nominally $St = 50$), these are $St = 10$, 30, 50, 100, and 150.

The uncontrolled case shows the shedding of a nearly two-dimensional vortex structure associated with the Kelvin-Helmholtz instability. This structure only exists in a short region before being dissipated quickly into smaller scale turbulence. Strong reverse flow within the LSB transports some turbulent structures upstream (colored in blue), feeding the transitional mechanisms.

At the lowest forcing frequency, $St = 10$, there is a slight increase in the size of the shed vortex structure. Otherwise, the transition process and location are largely unchanged. An indicator of this is the development of long-wavelength distortions in the shed vortex structure. This indicates that the forced two-dimensional mode is not amplified to the point at which it dominates the local flow field. In contrast at $St = 30$, these long wavelength modes are suppressed. Transition occurs through the development of a complex three-dimensional instability, which cause the transition point to move upstream. The strong development of short-wavelength three-dimensional instabilities on a forced LSB has been documented experimentally by Lang *et al.*[50].

At the most amplified frequency, $St = 50$, a strong train of coherent vortices are shed within the boundary layer.

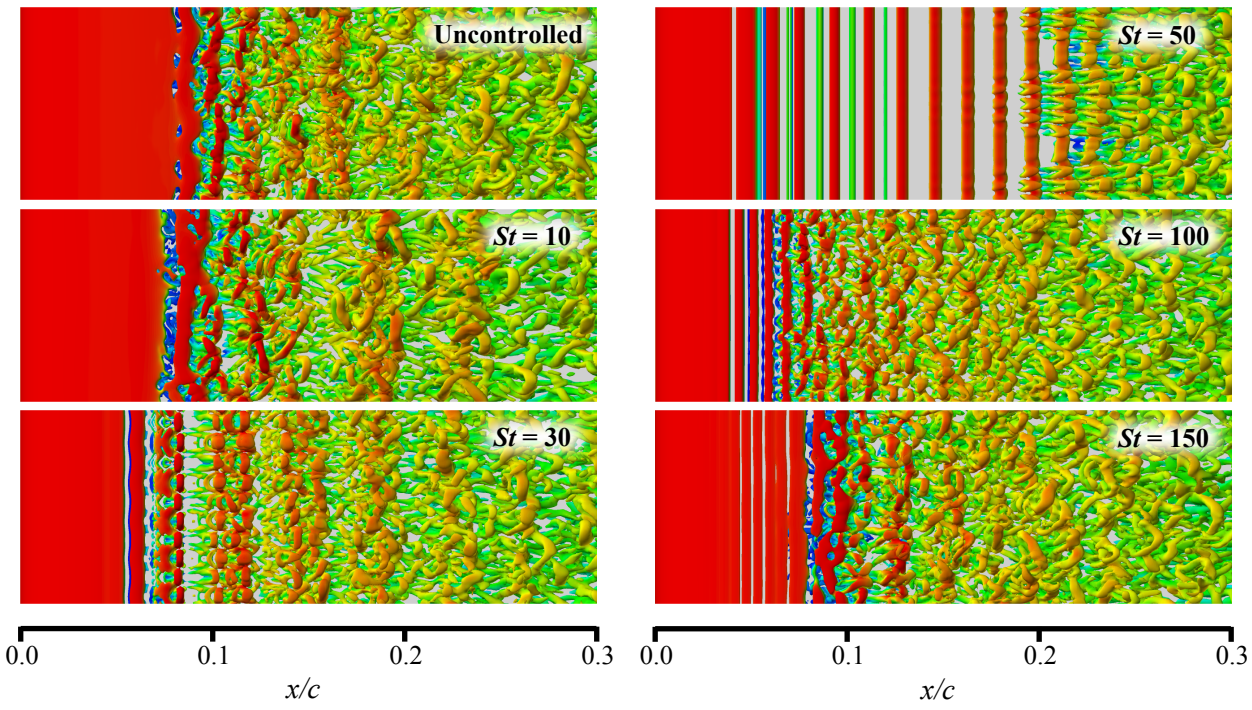

FIG. 6. Effect of sinusoidal forcing frequency on the leading edge flow structure. Iso-surfaces of q-criterion colored by local velocity magnitude, flow is left to right.

There are a number of unique features that are observed in this situation. First, the strong amplification of the forcing frequency completely suppresses all long wavelength disturbances that would otherwise develop within the LSB. This creates a highly two-dimensional flow field. Second, these coherent vortex structures interact with the wall and generate opposite-sign vortex structures (highlighted in green due to their lower velocity magnitude) these structures quickly dissipate and do not appear to have any role in the transition process. The interaction with the wall also suppresses the vortex pairing mechanism as shown in other studies of forced LSBs[17]. Transition finally occurs much further downstream ($x/c = 0.22$) through a short wavelength instability on the vortex similar to $St = 30$. However, in this case this secondary instability develops spatially in a convective manner as opposed to the rapid local growth observed at $St = 30$. This unique behavior has also been encountered for the case of a curved plate by Balzer[51]. It should be noted that the source of noise amplified by this secondary convective instability is a grid partition used for code parallelization. Additional simulations were performed to show that the transition could be delayed slightly by increasing the number of sub-iterations and/or number of overlapping planes. However, since this is the only source of three-dimensional noise in this region, it could not be completely removed and the simulation conditions were maintained in order to remain consistent with the other flow cases.

At the higher frequencies, $St = 100$ and 150, it can be seen that vortex shedding still locks on to the forcing frequency despite the fact that it is no longer tuned to the most amplified frequency ($St = 50$). At $St = 100$ transition is moved upstream, similar to $St = 30$, where small-wavelength three-dimensional instabilities appear to dominate the transition process. The spanwise wavelength of these structures is shorter in accordance with the smaller shear layer structures (compared to $St = 30 - 50$), indicating that the wavelength scales with the vortex core size and that it is likely associated with the elliptic instability[52]. At $St = 150$, small shear-layer vortices are visible corresponding to the higher forcing frequency. However, in this case the vortices eventually coalesce into a larger structure. This structure transitions though a process which appears similar to the uncontrolled flow whereby longer wavelength modes are seen to develop. In this case it appears that although coherent structures develop, locked on to the forcing frequency, they are not sufficiently amplified and have only a minimal effect on the development of the LSB.

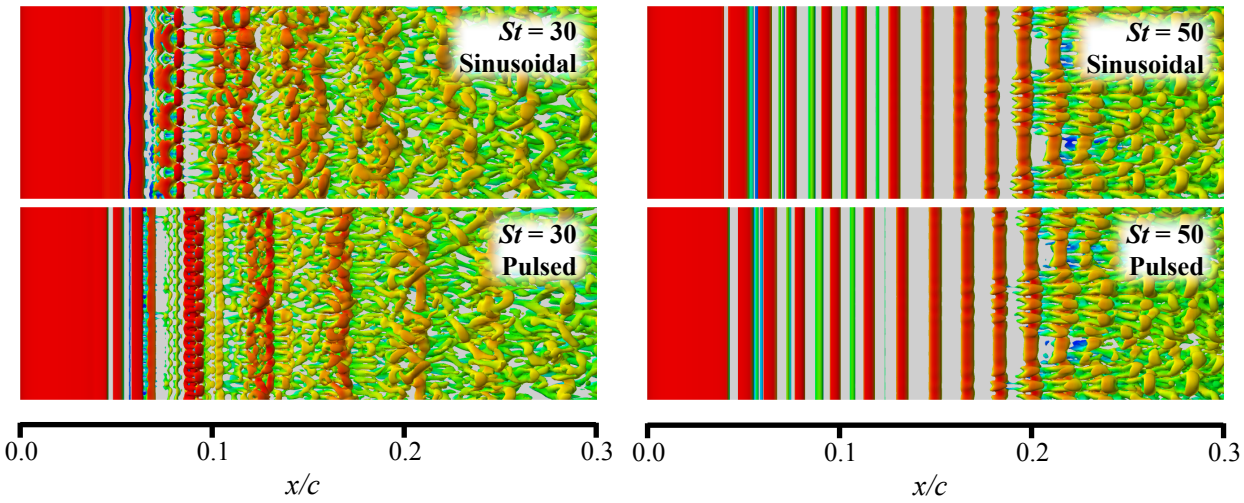

FIG. 7. Effect of forcing waveform on the leading edge flow structure. Iso-surfaces of q-criterion colored by local velocity magnitude, flow is left to right.

2. *Sinusoidal vs. Pulsed Forcing*

The previous data clearly shows that the effectiveness of high-frequency actuation lies in the ability to change the behavior of the LSB through the introduction of energy which is amplified by the primary instability mechanism. Depending on the relationship of the input frequency to the most amplified frequency, the transition point is moved upstream or downstream based on the nature of secondary instabilities present on the vortex structures. It is also instructive to understand the response of the LSB to forcing with a pulsed waveform. As discussed earlier, pulsed waveforms not only introduce energy at the pulsing frequency, but also at the odd super-harmonics. In the case of an unsteady event in which the LSB changes size, it may be advantageous to seed the LSB with energy in a wider frequency band in order to take advantage of the shifting characteristics of the LSB. Figure 7 shows a top-down view of q-criterion comparing the effect of waveform on the flow response. The purpose of this is to illustrate that at the most amplified frequency ($St = 50$) there is virtually no difference between sinusoidal and pulsed forcing. The primary mode is amplified considerably more than the super-harmonics and the final response is essentially identical. However, when the forcing frequency is lower than the most amplified ($St = 30$ in this case) there are significant differences. It is known from studying the uncontrolled flow field that both the primary mode ($St = 30$) and the $n = 3$ super-harmonic ($St = 90$) are both amplified. Looking at the size of the shed structures for the pulsed case at $St = 30$ it can been seen that shedding in the initial portion of the shear layer locks on to the $n = 3$ or $St = 90$ mode. These flow structures then merge into a larger structure that transitions to turbulence through a short wavelength, three-dimensional, mechanism.

To better illustrate this process, Fig. 8 shows contours of span-averaged vorticity overlaid with iso-lines of q-criterion. This illustrates the shedding and merging process of the $St = 90$ mode and the $St = 30$ mode. In this process, for each pulse at $St = 30$, three vortices develop in the shear layer. The latter two vortices merge together as the third vortex appears to dissipate into the near-wall vorticity, this results in a single larger structure which develops at a rate of once per pulse. This structure, however, dissipates rather quickly as seen in the three-dimensional representation in Fig. 7.

3. *Effects on the Time Mean Flow*

Table I shows the improvement in lift-to-drag ratio for the various forcing conditions discussed here. Of note is the finite range of effective frequency which approximately corresponds to the range of amplified frequencies as predicted in the linear stability analysis (Fig. 5). For the cases which are effective at increasing the lift-to-drag ratio, this is typically associated with an approximate 3-4% increase in lift along with a 15-20% reduction in drag. The drag reduction is associated with a strong reduction (25-30%) in the pressure drag and an increase (5-10%) in the friction drag. For properly tuned forcing, this indicates that control is beneficial even in static conditions pre-stall through improved efficiency. However, the response to control as a function of forcing frequency is abrupt and depends strongly

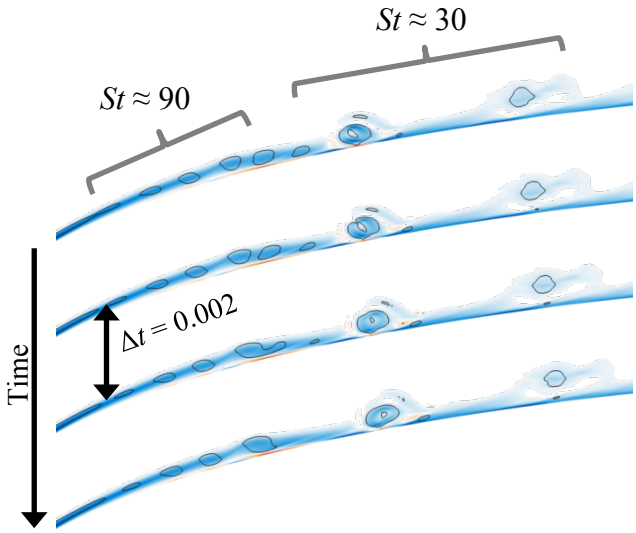

FIG. 8. Contours of instantaneous, span-averaged, ω_z overlaid with iso-lines of q-criterion showing the merging process of shear layer vortices for case of pulsed control at $St = 30$.

TABLE I. Time-averaged force coefficients (including pressure ($C_{d,p}$) and friction ($C_{d,f}$) drag) for the various cases at $\alpha = 8^\circ$.

St	Waveform	C_l	$C_{d,p}$	$C_{d,f}$	C_d	C_l/C_d
Uncontrolled		0.80 -	0.017 -	0.0080 -	0.025 -	31.9 -
10	Sinusoidal	0.81 +2%	0.016 -8%	0.0080 +1%	0.024 -5%	34.2 +7%
30	Sinusoidal	0.83 +3%	0.011 -35%	0.0084 +6%	0.020 -22%	42.0 +32%
50	Sinusoidal	0.84 +4%	0.013 -26%	0.0086 +8%	0.021 -15%	39.2 +23%
100	Sinusoidal	0.83 +3%	0.012 -30%	0.0084 +6%	0.020 -18%	40.3 +26%
150	Sinusoidal	0.81 +1%	0.015 -10%	0.0079 +0%	0.023 -7%	34.5 +8%
30	Pulsed	0.83 +3%	0.014 -21%	0.0083 +4%	0.022 -13%	37.9 +19%
50	Pulsed	0.83 +3%	0.012 -30%	0.0086 +8%	0.021 -18%	40.2 +26%

on the transitional mechanisms present within the bubble. The mechanisms do appear to extend the range of effective frequency compared to that predicted solely by the linear stability analysis (Fig. 5).

These time-mean flow fields are computed over a period of four characteristic times after control has been on for eight characteristic times. The drag force transient is on the order of one-half a characteristic time whereas the lift transient is on the order of five characteristic times. This indicates that the drag reduction is linked to the shortening of the LSB and manipulation of the turbulent boundary layer whereas the lift increase requires a global adjustment of airfoil circulation in accordance with the effective airfoil shape change.

The time mean wall pressure and wall shear for the uncontrolled and select cases of sinusoidal forcing are shown in Fig. 9. For the case in which forcing is tuned to the most amplified frequency ($St = 50$), the effect of coherent vortex shedding is seen in both the wall pressure and the wall shear. The wall pressure shows an increase in peak suction and a corresponding decrease in the plateau associated with the LSB. Coherent vortex shedding results in a secondary region of elevated suction that eventually dissipates once transition occurs. The wall shear shows a strong reduction in the region of reverse flow which indicates the extent of the time mean LSB. Time-mean wall shear increases in the presence of coherent vortex shedding to an intermediate value which represents the mean of the fluctuations occurring beneath the passing vortices. Eventually, transition occurs resulting in a second spike in wall shear which eventually recovers to the turbulent trend that extends to the trailing edge.

In the case of frequencies which are only moderately amplified ($St = 30$ and $St = 100$), the main effect of control is moving the transition location upstream. Decreasing the size of the time-mean LSB has a more beneficial effect in reducing the pressure drag as there is no region of suction associated with the coherent vortex regime. Interestingly, even though transition is moved upstream, there is nearly an identical increase in the friction drag for these cases as there is for the cases of coherent vortex shedding. This is due to the fact that when transition occurs, in the cases with coherent vortex shedding, it is associated with a high-shear process which makes up for the benefit associated with the temporary reduction in skin-friction due to the coherent vortex structures. For the frequencies furthest from the

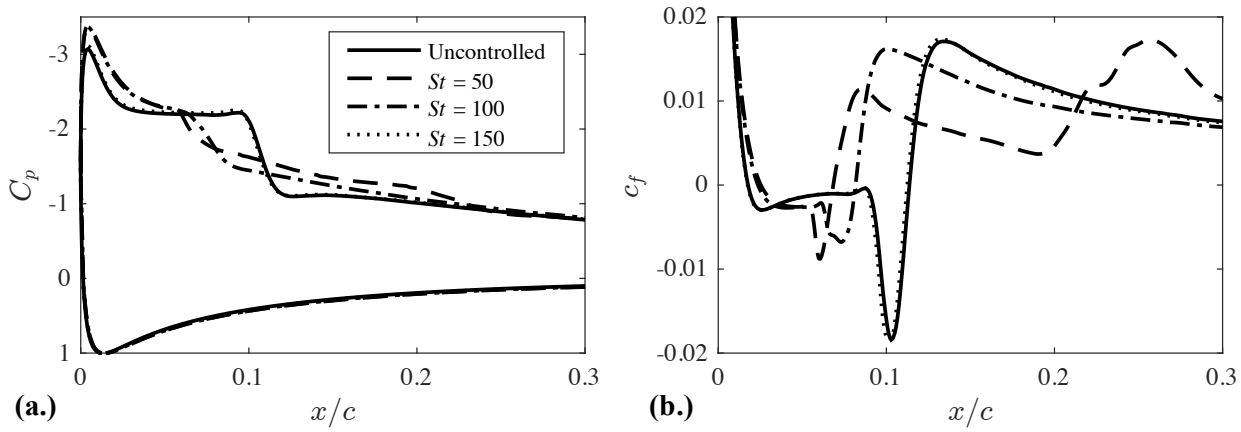

FIG. 9. Time-mean wall-pressure (a.) and skin friction (b.) coefficients at $\alpha = 8^\circ$ for the uncontrolled case and select cases of sinusoidal forcing.

most amplified (only $St = 150$ is included in Fig. 9) only minimal effects are observed when compared to uncontrolled flow.

4. Implications for Unsteady Separation

Early analyses, such as those discussed by Tani[48], described the existence of an LSB as a balance between the upstream pressure force (effectively acting on the bubble height) and the entrainment of momentum in the transitional region of the bubble. This analysis was extended to the case of bubble bursting by considering the scenario in which the upstream pressure force is no longer matched by the entrainment of momentum. For the case of a dynamic motion, specifically pitching to high α, the bubble will temporarily experience very strong pressure gradients and hence LSB bursting is likely. As shown here, forcing (when operated within a specified frequency range) energizes the bubble and significantly reduces its height. This reduction in height is expected to mitigate the strength of the upstream pressure force and put the bubble in a more stable position, as would be suggested by various bursting parameters[48, 53].

The forcing amplitude used in the current study is purposefully set at a low value in order to utilize convective instability mechanisms and to reduce energy costs to the controlled system. However, such a low amplitude introduces a strong sensitivity to forcing frequency as discussed previously. This frequency is linked to the velocity and length scales of the LSB and is expected to change during dynamic maneuvers as length scales adjust and local free-stream velocities change. Therefore, forcing at a fixed frequency may or may not be effective during an unsteady maneuver depending on the severity of the flow deviation and the width of the effective frequency range. This suggests that multi-frequency inputs such as pulsed waveforms may be more robust to control over a wider range of motions.

C. Uncontrolled Dynamic Stall

Starting at $\alpha = 8^\circ$ the airfoil is pitched up using the prescribed motion and parameters discussed previously. At this Reynolds number the dynamic stall process develops primarily from the bursting of a contracted LSB. This bursting process results in the development of a dynamic stall vortex (DSV) which is initiated from the LSB and sheds downstream. In this work, the focus is on the onset of dynamic stall (i.e. the initial development of the DSV) and details concerning the development of the DSV past $x/c \approx 0.25$ are mostly ignored. Figure 10 shows the general process of DSV development using contours of entropy. As the bubble reattachment point begins to move downstream ($\alpha \approx 14.5^\circ$) a coherent vortex structure begins to emerge. The expansion of the region of reversed flow due to the bursting process engulfs a portion of the local turbulent boundary layer. This develops into a turbulent structure which is continually fed from the leading edge shear layer. The DSV appears to develop coherence at $\alpha \approx 18^\circ$. Above this angle the DSV continues to grow in size and advect downstream.

Figure 11 shows wall pressure traces at $x/c = 0.01$ and $x/c = 0.25$ to illustrate the collapse of airfoil suction and the pressure signature created by the convecting DSV. The point at which the DSV passes $x/c = 0.25$ indicates the approximate onset of moment stall due to the movement of the suction peak downstream of the aerodynamic center.

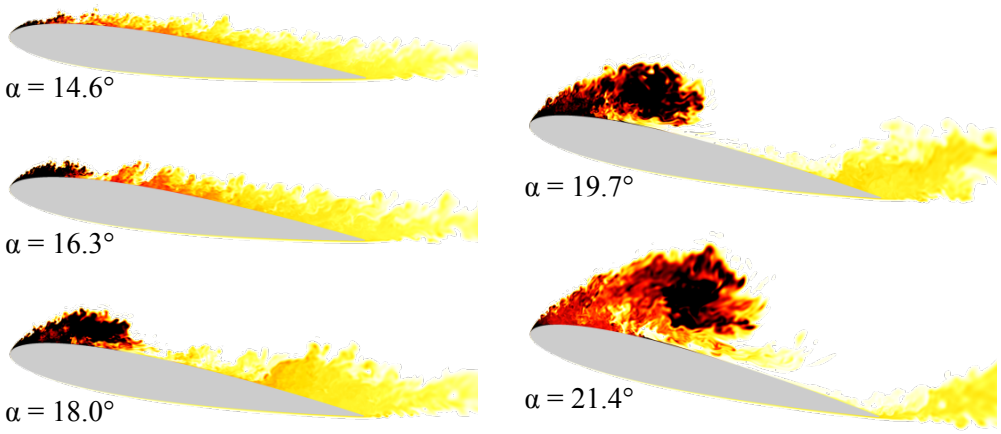

FIG. 10. Contours of entropy showing the onset of dynamic stall for the uncontrolled pitching simulation. A video of this process is included in the supplementary material[54].

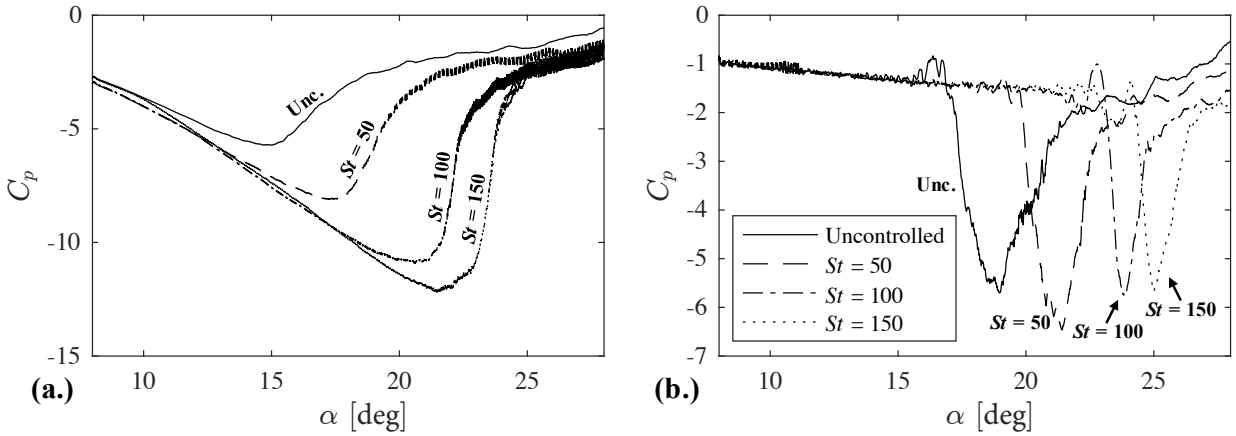

FIG. 11. Span-averaged wall pressure coefficient at $x/c = 0.01$ (a.) and $x/c = 0.25$ (b.) for the uncontrolled simulation and for control with sinusoidal forcing.

The left-most figure in Fig. 12 shows an $x - \alpha$ contour of the suction surface skin-friction coefficient during the dynamic stall process. The LSB is shown as a region of nearly stagnant reversed flow (white), terminated by a short region of strong reversed flow (blue) right before reattachment. This feature contracts from a length of $s/c \approx 0.1$ at $\alpha = 8°$ to $s/c \approx 0.07$ at $\alpha = 13.5°$ at which point the reattachment point begins to move downstream. This representation also tracks the development of the turbulent separation (black dashed line) which develops from the trailing edge. This is first seen at approximately $\alpha = 13.5°$ and propagates to its most upstream point of $x/c = 0.7$ at $\alpha = 17°$. The events leading up to the onset of dynamic stall in this uncontrolled case are discussed in considerably more detail by Visbal and Garmann[45].

D. Dynamic Stall Control

1. *Sinusoidal Forcing*

The ability for low amplitude high-frequency unsteady forcing to delay the onset of dynamic stall is investigated for six different parameter sets. The first is an investigation of sinusoidal forcing. It is expected based on increased boundary layer edge velocity and reduced LSB length scales that at higher angles the range of most amplified frequency will increase proportional to α. Therefore, simulations are performed with frequencies of $St = 50$, 100, and 150 starting with the solutions at $\alpha = 8°$ where control has been on for some time.

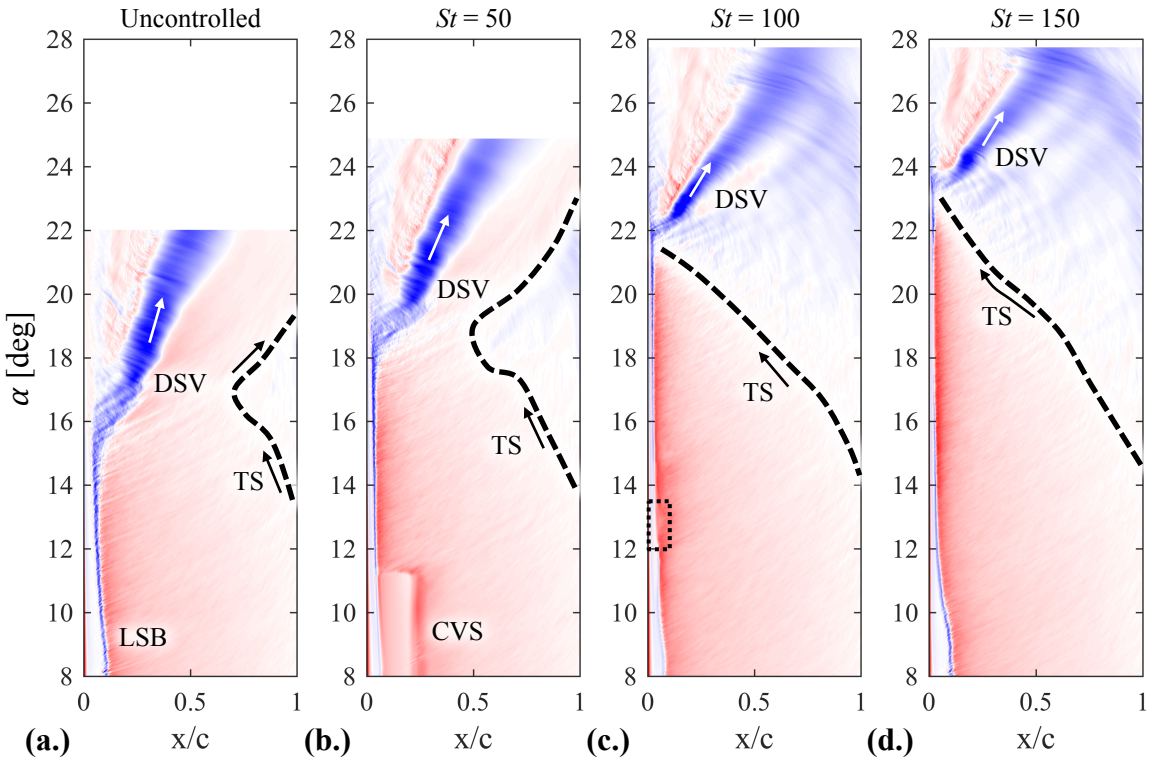

FIG. 12. $x - \alpha$ diagrams of span-averaged suction surface skin friction coefficient for the uncontrolled simulation and control with sinusoidal forcing. The black dashed line indicates the approximate location of turbulent separation (TS).

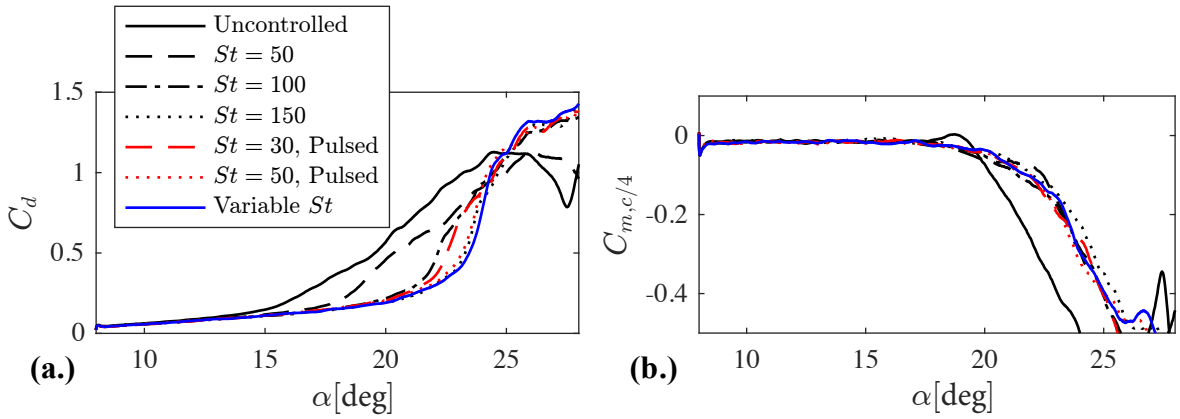

FIG. 13. Drag (a.) and pitching moment (b.) force coefficients for each of the seven pitching simulations.

Figures 11, 12, and 13 each show a continued delay of the onset of dynamic stall as forcing frequency is increased. Forcing at $St = 50$, 100, and 150 result in delays of suction peak collapse (as measured at $x/c = 0.01$, Fig. 11a) to $\alpha = 17.5°$, 20.5°, and 21.5°, respectively, from 15.0° in the uncontrolled case. This coincides with a delay in the development and propagation of the DSV as shown in Fig. 11b. Of note in Fig. 11 are the rate changes which occur with more effective control. The suction peak collapse and the initial propagation speed of the DSV are each shown to increase as dynamic stall is delayed to higher α.

$x - \alpha$ contours in Fig. 12 are also shown for the three cases of sinusoidal forcing. The development of the DSV wall-shear signature is delayed in accordance with the evidence from the wall pressure coefficient. This representation shows that as the bubble bursting is mitigated that turbulent separation is allowed to propagate further upstream as the airfoil pitches to higher α. For forcing at $St = 50$ turbulent separation propagates to mid-chord before reversing direction in accordance with the downstream movement of the DSV. For higher forcing frequency the turbulent

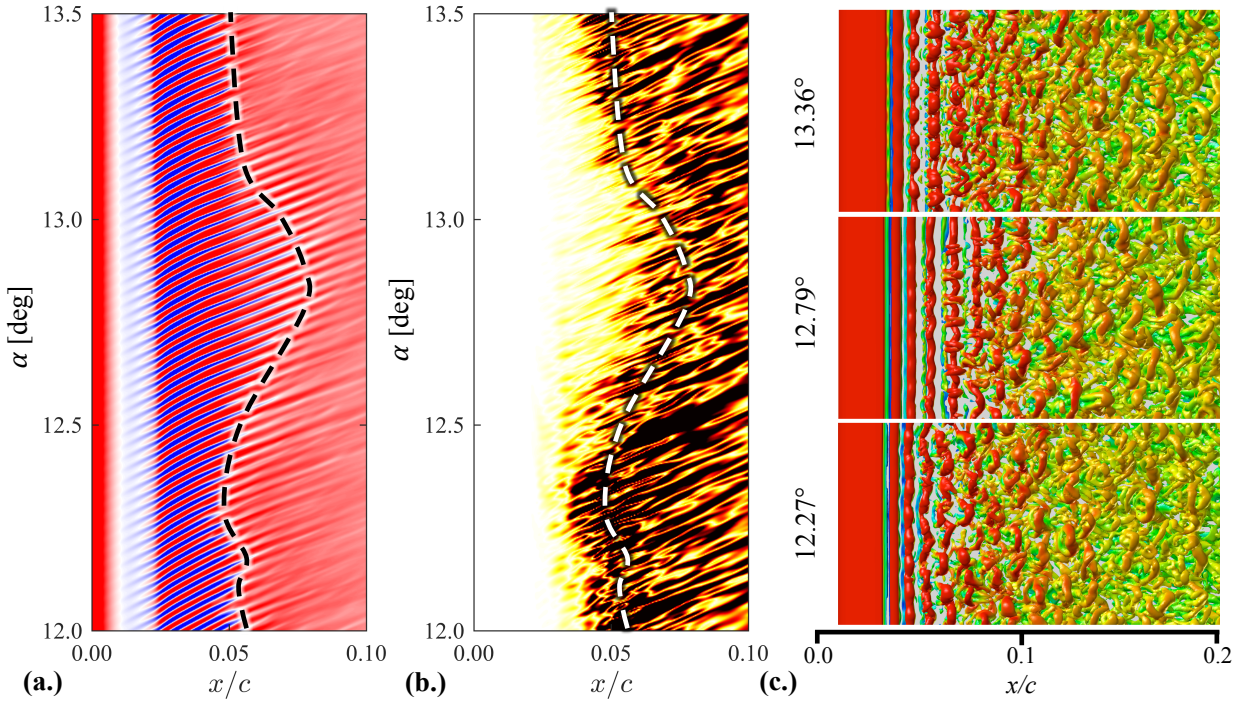

FIG. 14. Figures representing vortex shedding and transition movement for sinusoidal forcing at $St = 100$. (a.) $x - \alpha$ of skin friction coefficient. Domain corresponds to the box shown in Fig. 12. (b.) $x - \alpha$ of $|\omega_x|$ (black corresponds to $|\omega_x| = 100$). (c). Iso-surfaces of q-criterion.

separation propagates up to the LSB. For these higher frequency cases, it appears that the development of the DSV occurs due to the interaction between the turbulent separation and the LSB. This interaction is associated with a more abrupt collapse of leading edge suction and a faster movement of the DSV downstream.

An additional feature highlighted in Fig. 12 is the rapid cessation of coherent vortex shedding (labelled CVS, in Fig. 12) for forcing at $St = 50$. At approximately $\alpha = 11.5°$ the region of relatively low wall shear associated with coherent shedding rapidly disappears as transition moves upstream. This is consistent with the primary transition mechanism switching from a convective instability to an absolute instability. This process is discussed in more detail in the next section in the context of pulsed forcing at $St = 50$.

When forcing is instead tuned to $St = 100$ a region of increased receptivity develops in the vicinity of $\alpha = 13.0°$. This region is outlined in Fig. 12 and is expanded in Fig. 14a to show the detailed signature of the vortex shedding. Figure 14b also includes a $x-\alpha$ diagram of span-averaged x-vorticity (ω_x, corrected to the stationary frame of reference with x being the chordwise direction). This representation highlights the onset of three-dimensional structures associated with the secondary instability mechanism and the transition to turbulence. Near $\alpha = 12.8°$ the signature of the shed vortices temporarily extend downstream. This indicates that at this α the airfoil is temporarily most receptive to forcing at $St = 100$, in agreement with the expectation that the most amplified frequency increases with α. This downstream extension coincides with a downstream delay of the development of ω_x, indicating that the growth rate of the secondary instability has been temporarily reduced. Figure 14c includes iso-surfaces of the turbulent structures (colored by local velocity magnitude) at three instances within this region of α. It is seen that at $\alpha = 12.8°$ the amplitude of the three-dimensional structures are temporarily reduced in conjunction with a slight delay of transition.

Force histories (Fig. 13) illustrate the effect of control most clearly in terms of the delay in the rise of the drag coefficient. For the more effective cases the eventual drag rise is very rapid. Interestingly, the development of a nose-down pitching moment is nearly identical for all control cases as compared to the uncontrolled case. This is due to the thickening of the turbulent boundary layer prior to stall which increases the loading over the aft portions of the suction surface. When the DSV eventually appears, both effects are of similar order and no clear response in the moment coefficient is observed in relation to the DSV development and propagation.

For the most effective case of sinusoidal forcing, at $St = 150$, the development of the dynamic stall process is illustrated in Fig. 15 using contours of entropy. In comparison with the uncontrolled dynamic stall (Fig. 10) the turbulent boundary layer is much thicker prior to DSV development. In this case, turbulent separation has propagated nearly to the leading edge resulting in reversed flow over much of the airfoil chord. As the DSV reaches coherence

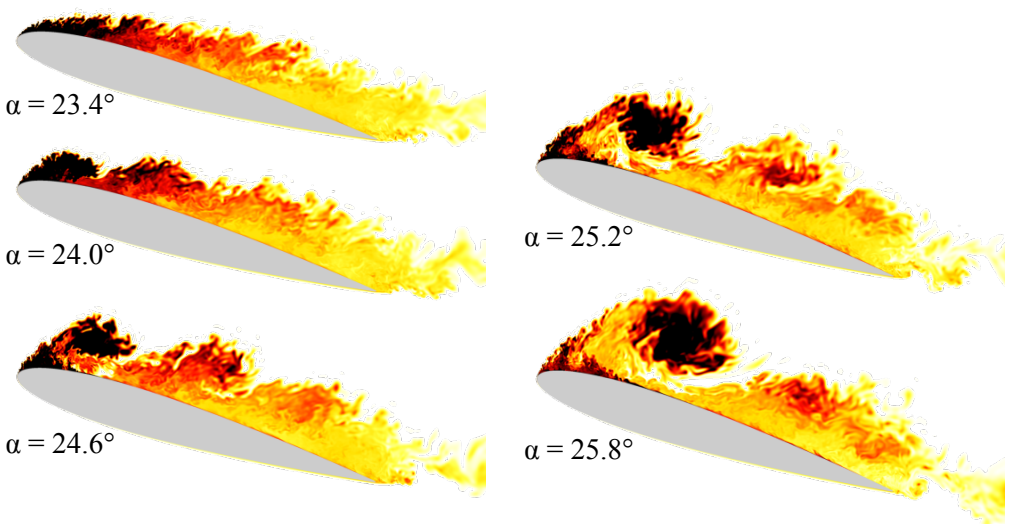

FIG. 15. Contours of entropy showing the onset of dynamic stall for sinusoidal forcing at $St = 150$. A video of this process is included in the supplementary material[54].

near $\alpha = 24.0°$ a second, weaker, shear layer vortex (SLV) develops from the separated turbulent boundary layer. Both vortices convect downstream simultaneously, however the strength of the SLV appears to diminish as the size of the DSV grows. Of note here is the much more rapid development of the DSV at these high angles compared to the uncontrolled case. The same process of a developing DSV propagating to nearly the quarter-chord location occurs in less than $\Delta\alpha = 2°$ compared to nearly $\Delta\alpha = 5°$ for the uncontrolled case. The rapid development of the DSV in the controlled scenario corresponds to the rapid increase in drag coefficient shown in Fig. 13.

2. Pulsed Forcing

In accordance with the parameters investigated at the static condition of $\alpha = 8°$, pitching simulations are also performed with pulsed forcing at $St = 30$ and $St = 50$. These waveforms contain frequency content at the odd super-harmonics of the pulsing frequency ($n = 3, 5, 7, \ldots$) only, with decreasing amplitude at each harmonic proportional to n^{-1}. Of note is the fact that both forcing schemes introduce energy at $St = 150$ as this is the $n = 5$ super-harmonic of $St = 30$ and the $n = 3$ super-harmonic at $St = 50$.

For these cases of pulsed control the force histories (Fig. 13) show comparable effectiveness at delaying the onset of dynamic stall as sinusoidal forcing at higher frequencies. Focusing on the drag coefficient specifically, pulsed forcing at $St = 50$ is only slightly less effective than sinusoidal forcing at $St = 150$ and pulsed forcing at $St = 30$ out performs sinusoidal forcing at $St = 100$, but is less effective compared to pulsed forcing at $St = 50$.

$x - \alpha$ contours of skin friction coefficient for the two cases of pulsed forcing are presented in Fig. 16. In comparison to sinusoidal forcing many of the same features are present including DSV development, the extended region of CVS when forcing is applied at $St = 50$, and upstream propagation of the turbulent separation. For pulsed forcing at $St = 50$, a region of the $x - \alpha$ contour near $\alpha = 12.0°$ is expanded in Fig. 17a. Within this domain, the wall shear signature shows evidence of vortex shedding initially occurring at the $n = 3$ super-harmonic ($St = 150$) with a merging process that takes place between the system of three vortices resulting in a single structure at $St = 50$. This process is nearly identical to that described for the static case at $\alpha = 8°$ with pulsed forcing at $St = 30$ (Fig. 8). Detailed in Fig. 17b and Fig. 17c is the abrupt cessation of the region of extended CVS. $x - \alpha$ contours of ω_x show that at approximately $\alpha = 12.1°$ three-dimensional structures develop on the shed vortex at approximately $x/c = 0.04$ and convect downstream with the vortex structure. This same representation shows a much slower upstream progression of transition starting at $x/c = 0.22$ which merges with the downstream propagation at $x/c = 0.19$, slightly above $\alpha = 12.3°$. This same process is illustrated in Fig. 17c using iso-surfaces of q-criterion. Each of these snapshots are separated by $\Delta t = 0.02$ (the period of actuation), this shows that transition first develops on the most upstream vortex and is convected downstream on that same vortex.

Because this secondary instability develops on the vortex rather than within the braid region between vortices, it is expected that it is associated with the elliptical instability that develops on vortices deformed by an external strain

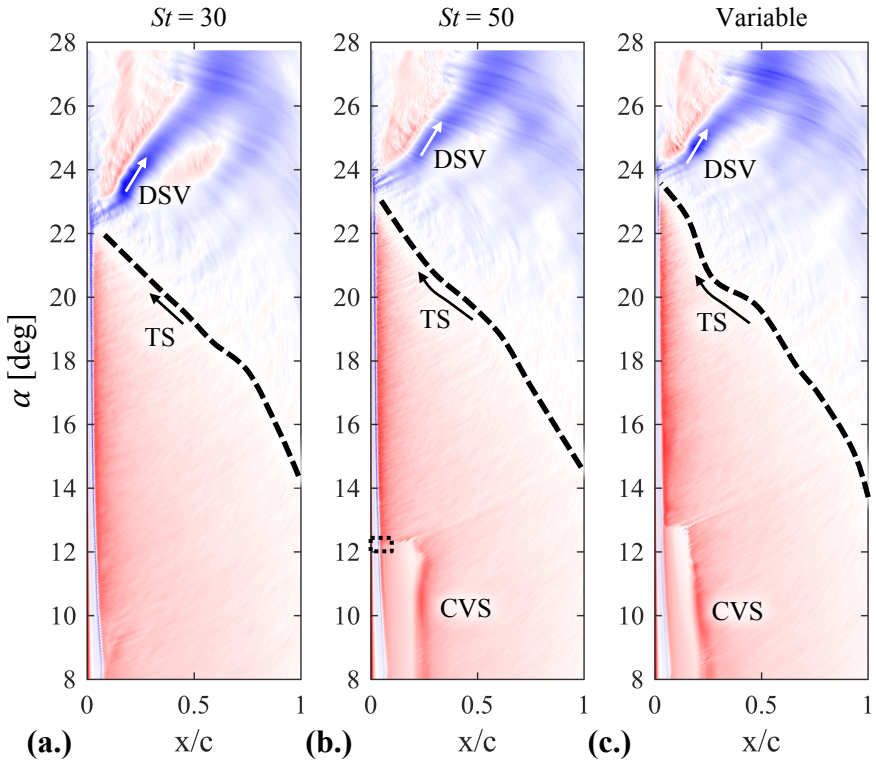

FIG. 16. $x-\alpha$ diagrams of span-averaged suction surface skin friction coefficient for the cases of control with pulsed forcing and the case of variable frequency control.

field[51, 52, 55]. The growth rate of this instability is linked to the strength of the vortex and the relative proximity of the vortex to the airfoil surface. Therefore, this apparent transition from convective to absolute instability occurs when the time-scale of the instability growth rate becomes significantly faster than the convection velocity of the vortices. When this occurs, the instability serves as a mechanism for by-pass like transition instead of a slowly developing feature on the convecting vortices. Further work is required to fully understand this feature.

3. Variable Frequency Control

The results to this point fit a model suggesting that continually energizing the LSB prevents the bursting event which is shown to initiate the DSV in the uncontrolled configuration. This continual energizing is complicated by the fact that the range of amplified frequencies shifts towards higher values as the airfoil pitches up. To quantify this increase with α, eq. 8 introduces a scaling argument based upon the momentum thickness and the boundary layer edge velocity at separation to extrapolate the most amplified frequency measured at the initial static condition.

$$St\left(\alpha\right) = St_0 \frac{\theta_{s,0}}{\theta_s\left(\alpha\right)} \frac{U_{e,s}\left(\alpha\right)}{U_{e,s,0}} \tag{8}$$

Using instantaneous span-averaged solutions, the most amplified frequency has been estimated from the uncontrolled pitching simulation using eq. 8. The momentum thickness (θ_s) and boundary layer edge velocity ($U_{e,s}$) at separation are extracted from the instantaneous, span-averaged solutions up to the point at which the LSB bursts. Based upon the nominal effective frequency at $\alpha_0 = 8°$ of $St_0 = 50$, eq. 8 is applied to estimate the most amplified freqeuncy for higher α (Fig. 18, black dots). Applying eq. 8 to $St = 30$ and $St = 100$ (each shown to shorten the length of the LSB at $\alpha = 8°$) a gray domain is highlighted in Fig. 18 which outlines the possible extent of the range of effective frequency. Included in Fig. 18 are horizontal dashed lines that locate the sinusoidal forcing cases discussed previously, as well as vertical dotted lines that indicate the nominal location of dynamic stall (DS, in Fig. 18) for the uncontrolled and the $St = 150$ cases.

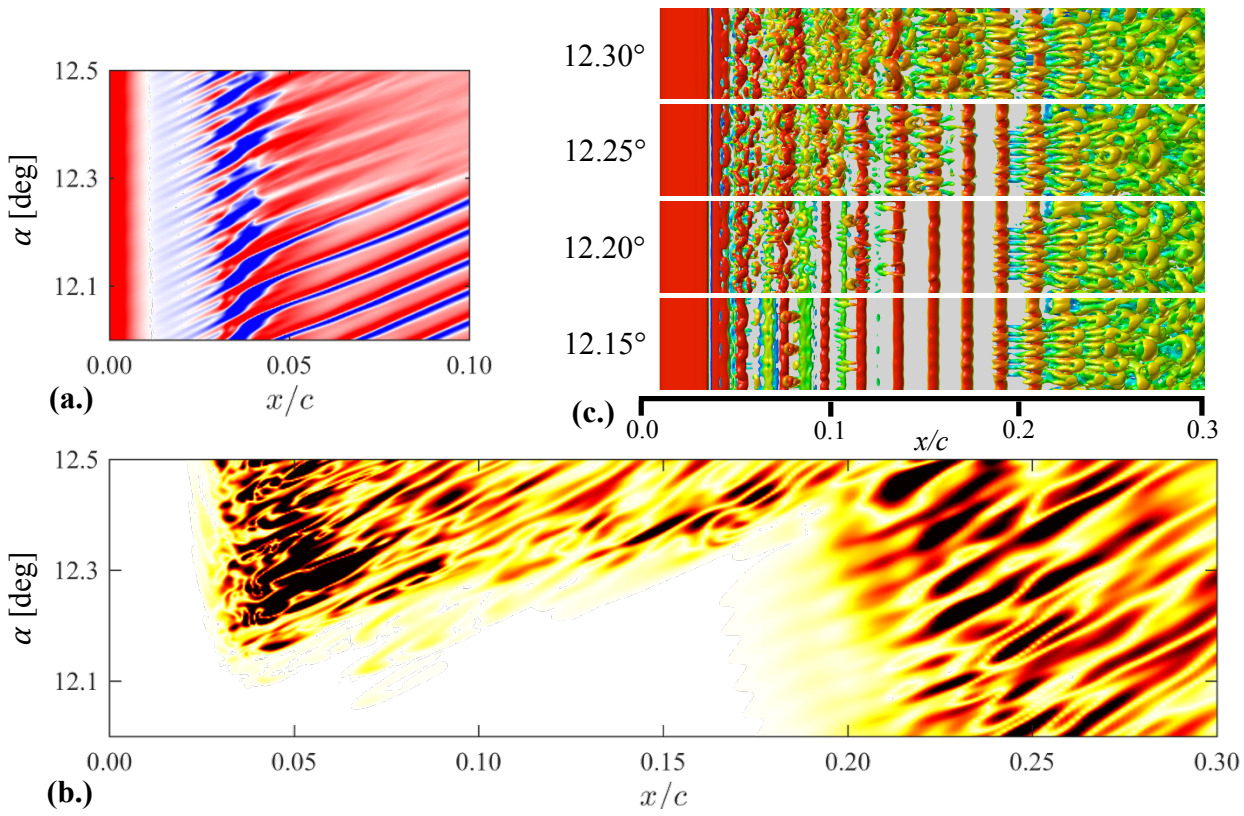

FIG. 17. Figures representing vortex shedding and transition movement for pulsed forcing at $St = 50$. (a.) $x - \alpha$ of skin friction coefficient. Domain corresponds to the box shown in Fig. 16. (b.) $x - \alpha$ of $|\omega_x|$ (black corresponds to $|\omega_x| = 100$). (c). Iso-surfaces of q-criterion.

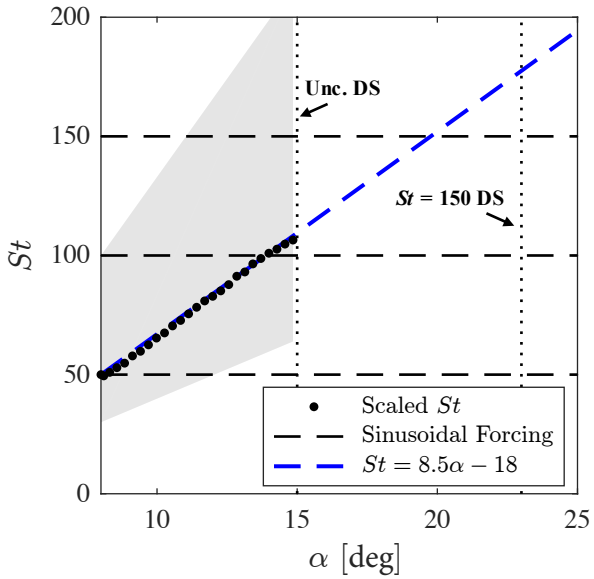

FIG. 18. Schematic showing the estimated relationship between the most effective St and α based upon the relationships in eqs. 8 and 9. Vertical dotted lines represent approximate locations for dynamic stall in the uncontrolled and sinusoidal forcing at $St = 150$ cases.

To validate the model of control effectiveness, a final simulation is run in which the forcing frequency (starting at $\alpha = 8^\circ$ and $St = 50$) dynamically adjusts as a function of α. Frequency is linked to α through the fit in eq. 9 which is also included in Fig. 18.

$$St\,(t) = 8.5\alpha\,(t) - 18 \tag{9}$$

To implement this control approach, it is necessary to integrate the time-varying frequency to maintain a proper phase relationship as the frequency adjusts. This is implemented as shown in eqs. 10 and 11 where $F(t)$ corresponds to the time function in eq. 2.

$$\phi\,(t) = \pi \int_{t_0}^{t} St\,(t)\,dt \tag{10}$$

$$F\,(t) = sin^2\,(\phi\,(t)) \tag{11}$$

For the variable frequency simulation, $\alpha\,(t)$ (eq. 7) is analytically integrated in order to define the frequency as a function of time. This approach however could be generalized to any motion, through numerical integration, so long as a smooth estimate of the instantaneous α is available.

The results of the variable frequency simulation show a delay and eventual stall process nearly identical to the results for sinusoidal forcing at $St = 150$ and pulsed forcing at $St = 50$ as shown by the force histories in Fig. 13. Of note is that the variable frequency case actually exceeds a frequency of $St = 150$ in the region of $\alpha = 20^\circ$. The history of the drag coefficient shows a slight benefit to the continual tracking of the most amplified frequency. This is encouraging as the variable frequency approach is less reliant on trial and error concerning the receptivity of the LSB to forcing frequency and could be directly applied to other pitching motions. This also appears to suggest an upper limit for control effectiveness (at least at this forcing amplitude) with respect to frequency selection. A $x-\alpha$ diagram of wall skin-friction coefficient for the variable frequency case is also included on the right in Fig. 16. The slight delay in stall onset introduced by this method compared to pulsed forcing at $St = 50$ is visible. A slight extension of the region of CVS due to the tracking of the most amplified frequency is also present. These results suggest that exclusive use of the variable frequency approach may allow for further reduction in the energy cost of the control scheme.

V. CONCLUSION

High-fidelity simulations of low-amplitude high-frequency flow control applied to the case of dynamic stall on a NACA 0012 airfoil have been presented. At $Re_c = 2 \times 10^5$ the suction surface boundary layer, prior to stall, is characterized by a turbulent boundary layer which develops due to transition in a small LSB located near the leading edge. The LSB is shown to act as an amplifier to unsteady forcing through a strong convective instability mechanism present in the upstream portion of the bubble.

At the static condition of $\alpha = 8^\circ$ the receptivity of the bubble to sinusoidal forcing is investigated. Within a relatively wide range of forcing frequencies, the time-mean LSB shrinks and pressure drag is strongly decreased. This results in lift-to-drag increases on the order of $20 - 25\%$. This is shown to depend partly on bubble receptivity to forcing through the primary convective instability, but also to the behavior of a secondary short-wavelength spanwise instability that develops on the shear layer vortices. Pulsed forcing is also investigated. It is shown that at these forcing amplitudes, the LSB is primarily affected by the relation of the pulsing frequency and its odd super-harmonics to the range of amplified frequency.

Control is then applied to the case of a constant-rate pitch-up motion starting at $\alpha = 8^\circ$. For the uncontrolled case, the onset of dynamic stall occurs from the bursting of the leading edge LSB. At the point that the DSV develops turbulent separation at the trailing edge has only begun to develop and plays a minor role in the dynamic stall process. For sinusoidal forcing it is shown that a frequency of $St = 150$ is most effective at delaying leading edge separation. LSB bursting is delayed until the point at which the trailing edge turbulent separation propagates to the leading edge and the DSV forms. Pulsed control at $St = 50$ is shown to be nearly as effective as sinusoidal control at $St = 150$. $x-\alpha$ contours of the vortex shedding in the LSB show that at higher angles vortices are initially shed at the $n = 3$ super harmonic and merge to form a single structure at the pulsing frequency. This along with other observations suggests that the dynamic behavior of the LSB during the pitching motion is relatively unchanged in reference to the static pre-stall situation except for the increase in the most amplified frequency. This quasi-steady behavior in the LSB is due to the drastic separation in time scales between the LSB and the global airfoil motion.

With this model in mind, a scaling argument based upon local flow velocities and length scales in the LSB is devised to estimate the most amplified frequency as a function of α. A linear relationship between St and α is extracted and introduced into a variable frequency forcing scheme that dynamically adjusts the frequency as a function of α. This control scheme performs as well as the best cases of sinusoidal and pulsed forcing, indicating that an upper bound for control effectiveness has been reached.

When the sensitivity to frequency is properly taken into account, the control approach presented here offers an effective low-energy approach to dynamic stall control for situations in which LSB bursting is dominant. This would allow for the usage of large bandwidth actuators such as synthetic-jet and plasma actuators at higher flow speeds. Future work to determine the contribution of the LSB to the dynamic stall process as a function of increased Reynolds number and airfoil shape is necessary.

ACKNOWLEDGMENTS

This work was sponsored in part by AFOSR under Task FA9550-17RQCOR393 monitored by Dr. D. Smith and also by a grant of HPC time from the DoD HPC Shared Resource Centers at AFRL and ERDC. This research was performed while Dr. S. Benton held an NRC Research Associateship award at AFRL. Special thanks to Dr. D. Garmann for his help setting up and running FDL3DI.

REFERENCES

[1] W. J. McCroskey, "Unsteady airfoils," Annual Review of Fluid Mechanics **14**, 285–311 (1982).
[2] L. W. Carr, "Progress in analysis and prediction of dynamic stall," Journal of Aircraft **25**, 6–17 (1988).
[3] J. A. Ekaterinaris and M. F. Platzer, "Computational prediction of airfoil dynamic stall," Progress in Aerospace Sciences **33**, 759–846 (1997).
[4] N. D. Ham, "Some recent mit research on dynamic stall," Journal of Aircraft **9**, 378–379 (1972).
[5] W. Johnson and N. D. Ham, "On the mechanism of dynamic stall," Journal of the American Helicopter Society **17**, 36–45 (1972).
[6] J. M. Currier and K.-Y. Fung, "Analysis of the onset of dynamic stall," AIAA Journal **30**, 2469–2477 (1992).
[7] R. W. Prouty, "A state-of-the-art survey of two-dimensional airfoil data," Journal of the American Helicopter Society **20**, 14–25 (1975).
[8] W. J. McCroskey, K. W. McAlister, L. W. Carr, S. L. Pucci, O. Lambert, and R. F. Indergrand, "Dynamic stall on advanced airfoil sections," Journal of the American Helicopter Society **26**, 40–50 (1981).
[9] D. Greenblatt, "Active control of leading-edge dynamic stall," International Journal of Flow Control **2**, 21–38 (2010).
[10] D. Greenblatt and I. Wygnanski, "Dynamic stall control by periodic excitation, part 1: Naca 0015 parametric study," Journal of Aircraft **38**, 430–438 (2001).
[11] M. L. Post and T. C. Corke, "Separation control using plasma actuators: Dynamic stall vortex control on oscillating airfoil," AIAA Journal **44**, 3125–3135 (2006).
[12] C. G. Matalanis, B-. Y. Min, P. O. Bowles, S. Jee, B. E. Wake, T. M. Crittenden, G. Woo, and A. Glezer, "Combustion-powered actuation for dynamic-stall suppression: High-mach simulations and low-mach experiments," AIAA Journal **53**, 2151–2163 (2015).
[13] D. Greenblatt and I. J. Wygnanski, "The control of flow separation by periodic excitation," Progress in Aerospace Sciences **36**, 487–545 (2000).
[14] D. Postl, W. Balzer, and H. F. Fasel, "Control of laminar separation using pulsed vortex generator jets: direct numerical simulations," Journal of Fluid Mechanics **676**, 81–109 (2011).
[15] M. Embacher and H. F. Fasel, "Direct numerical simulations of laminar separation bubbles: investigation of absolute instability and active flow control of transition to turbulence," Journal of Fluid Mechanics **747**, 141–185 (2014).
[16] C. Bernardini, S. I. Benton, J-. P. Chen, and J. P. Bons, "Pulsed jets laminar separation control using instability exploitation," AIAA Journal **52**, 104–115 (2014).
[17] O. Marxen, R. B. Kotapati, R. Mittal, and T. Zaki, "Stability analysis of separated flows subject to control by zero-net-mass-flux jet," Physics of Fluids **27**, 024107 (2015).
[18] S. S. Collis, R. D. Joslin, A. Seifert, and V. Theofilis, "Issues in active flow control: theory, control, simulation, and experiment," Progress in Aerospace Sciences **40**, 237–289 (2004).
[19] M. R. Visbal, "Analysis of the onset of dynamic stall using high-fidelity large-eddy simulations," (American Institute of Aeronautics and Astronautics, 2014).

[20] M. R. Visbal, "Numerical exploration of flow control for delay of dynamic stall on a pitching airfoil," (American Institute of Aeronautics and Astronautics, 2014).

[21] M. R. Visbal, "Control of dynamic stall on a pitching airfoil using high-frequency actuation," (American Institute of Aeronautics and Astronautics, 2015).

[22] Miguel R. Visbal and Daniel J. Garmann, "High-fidelity simulations of dynamic stall over a finite-aspect-ratio wing," in *8th AIAA Flow Control Conference* (American Institute of Aeronautics and Astronautics, 2016).

[23] Miguel R. Visbal and Daniel J. Garmann, "Control of dynamic stall over a pitching finite-aspect-ratio wing," in *47th AIAA Fluid Dynamics Conference* (American Institute of Aeronautics and Astronautics, 2017).

[24] Miguel R. Visbal and Daniel J. Garmann, "Numerical investigation of spanwise end effects on dynamic stall of a pitching naca 0012 wing," in *55th AIAA Aerospace Sciences Meeting* (American Institute of Aeronautics and Astronautics, 2017).

[25] S. I. Benton and M. R. Visbal, "Investigation of high-frequency separation control mechanisms for delay of unsteady separation," (American Institute of Aeronautics and Astronautics, 2016).

[26] M. R. Visbal and D. V. Gaitonde, "High-order-accurate methods for complex unsteady subsonic flows," AIAA Journal **37**, 1231–1239 (1999).

[27] D. V. Gaitonde and M. R. Visbal, *High-Order Schemes for Navier-Stokes Equations: Algorithm and Implementation into FDL3DI*, Final Report AFRL-VA-WP-TR-1998-3060 (Air Force Research Laboratory, 1998).

[28] S. K. Lele, "Compact finite difference schemes with spectral-like resolution," Journal of Computational Physics **103**, 16–42 (1992).

[29] R. M. Beam and R. F. Warming, "An implicit factored scheme for the compressible navier-stokes equations," AIAA Journal **16**, 393–402 (1978).

[30] Marcel Vinokur, "Conservation equations of gasdynamics in curvilinear coordinate systems," Journal of Computational Physics **14**, 105–125 (1974).

[31] Joseph L. Steger, "Implicit finite-difference simulations of flow about arbitrary two-dimensional geometries," AIAA Journal **16**, 679–686 (1978).

[32] M. R. Visbal and D. V. Gaitonde, "On the use of higher-order finite-difference schemes on curvilinear and deforming meshes," Journal of Computational Physics **181**, 155–185 (2002).

[33] D. V. Gaitonde, J. S. Shang, and J. L. Young, "Practical aspects of higher-order numerical schemes for wave propagation phenomena," International Journal for Numerical Methods in Engineering **45**, 1849–1869 (1999).

[34] P. Alpert, "Implicit filtering in conjunction with explicit filtering," Journal of Computational Physics **44**, 212–219 (1981).

[35] D. V. Gaitonde and M. R. Visbal, "Further development of a navier-stokes solution procedure based on higher-order formulas," (American Institute of Aeronautics and Astronautics, 1999).

[36] M. R. Visbal and D. P. Rizzetta, "Large-eddy simulation on curvilinear grids using compact differencing and filtering schemes," Journal of Fluids Engineering **124**, 836–847 (2002).

[37] D. P. Rizzetta, M. R. Visbal, and G. A. Blaisdell, "A time-implicit high-order compact differencing and filtering scheme for large-eddy simulation," International Journal for Numerical Methods in Fluids **42**, 665–693 (2003).

[38] D. J. Garmann, M. R. Visbal, and P. Orkwis, "Comparative study of implicit and subgrid-scale model large-eddy simulation techniques for low-reynolds number airfoil applications," International Journal for Numerical Methods in Fluids **71**, 1546–1565 (2013).

[39] Chau-Lyan Chang, "Langley stability and transition analysis code (lastrac) version 1.2 user manual," (2004).

[40] Frédéric Alizard, Stefania Cherubini, and Jean-Cristophe Robinet, "Sensitivity and optimal forcing response in separated boundary layer flows," Physics of Fluids **21**, 064108 (2009).

[41] S. E. Sherer and M. R. Visbal, "Multi-resolution implicit large eddy simulations using a high-order overset-grid approach," International Journal for Numerical Methods in Fluids **55**, 455–482 (2007).

[42] See Supplemental Material at [URL will be inserted by publisher] for grid resolution study. ().

[43] N. J. Georgiadis, D. P. Rizzetta, and C. Fureby, "Large-eddy simulation: Current capabilities, recommended practices, and future research," AIAA Journal **48**, 1772–1784 (2010).

[44] Ugo Piomelli and Elias Balaras, "Wall-layer models for large-eddy simulations," Annual Review of Fluid Mechanics **34**, 349–374 (2002).

[45] Miguel R. Visbal and Daniel J. Garmann, "Analysis of dynamic stall on a pitching airfoil using high-fidelity large-eddy simulations," *AIAA Journal*, AIAA Journal **56**, 46–63 (2018).

[46] Y. Zhou and Z. J. Wang, "Absorbing boundary conditions for the euler and navier-stokes equations with the spectral difference method," Journal of Computational Physics **229**, 8733–8749 (2010).

[47] P. F. Lorber and F. O. Carta, "Airfoil dynamic stall at constant pitch rate and high reynolds number," Journal of Aircraft **25**, 548–556 (1988).

[48] Itiro Tani, "Low-speed flows involving bubble separations," Progress in Aerospace Sciences **5**, 70–103 (1964).

[49] O. Marxen, M. Lang, and U. Rist, "Vortex formation and vortex breakup in a laminar separation bubble," Journal of Fluid Mechanics **728**, 58–90 (2013).

[50] M. Lang, U. Rist, and S. Wagner, "Investigations on controlled transition development in a laminar separation bubble by means of lda and piv," Experiments in Fluids **36**, 43–52 (2004).

[51] Wolfgang Balzer, *Numerical Investigation of the Role of Free-Stream Turbulence on Boundary-Layer Separation and Separation Control*, Ph.D. thesis, The University of Arizona (2011).

[52] R. R. Kerswell, "Elliptical instability," Annual Review of Fluid Mechanics **34**, 84–113 (2002).

[53] S. S. Diwan, S. J. Chetan, and O. N. Ramesh, "On the bursting criterion for laminar separation bubbles," in *Sixth IUTAM Symposium on Laminar-Turbulent Transition*, edited by R. Govindarajan (2006) pp. 401–407.

[54] See Supplemental Material at [URL will be inserted by publisher] for video. ().
[55] Denis Sipp and Laurent Jacquin, "Windall instabilities in vortex pairs," Physics of Fluids **15**, 1861– (2003).